frontiers in Materials

ORIGINAL RESEARCH
published: 07 October 2020
doi: 10.3389/fmats.2020.567793

Microstructure and Mechanical Properties of BCC-FCC Eutectics in Ternary, Quaternary and Quinary Alloys From the Al-Co-Cr-Fe-Ni System

Daniel Röhrens[1], Niloofar Navaeilavasani[1], Oleg Stryzhyboroda[1], Fabian Swientek[2], Paul Pavlov[2], Dirk Meister[2], Amber Genau[3] and Ulrike Hecht[1]*

[1] Access e.V., Aachen, Germany, [2] Anton Paar Germany GmbH, Ostfildern-Scharnhausen, Germany, [3] Department of Materials Science and Engineering, The University of Alabama at Birmingham, Birmingham, AL, United States

This study aimed at understanding the structure and properties of dual-phase eutectics in ternary, quaternary, and quinary alloys of the Al-Co-Cr-Fe-Ni system. The alloys at case were i) $Ni_{48}Fe_{34}Al_{18}$, ii) $Ni_{44}Fe_{20}Cr_{20}Al_{16,}$ and iii) $Ni_{34.4}Fe_{16.4}Co_{16.4}Cr_{16.4}Al_{16.4}$. Samples in the form of cylindrical bars, diameter 10 mm × 150 mm, were produced by arc melting and suction casting from pure elements (>99.9 wt%). Bridgman solidification at low growth velocity was used to produce additional samples with large eutectic spacing and lamellae thickness of the two phases body-centered cubic (BCC)-B2 and face-centered cubic (FCC) in order to facilitate phase characterization by energy-dispersive X-ray analysis (scanning electron microscopy/energy-dispersive spectroscopy) and nano-indentation. In agreement with thermodynamic calculations, each of the phases was found to be multi-component and contain all alloying elements in distinct amounts. The mechanical properties of the individual phases were analyzed in relation to their composition using nano-indentation experiments. These measurements revealed some insights into "high-entropy effects" and their contribution to the elastoplastic response to indentation loading. Further analysis focused on as-cast as well as heat-treated samples comprising phase fraction measurements, micro-indentation, and miniature testing in three-point bending configuration. For optimum heat treatment conditions, a good balance of strength and ductility was obtained for each of the investigated alloys. Further work is necessary in order to assess their capability as structural materials.

Keywords: high entropy alloy, eutectic, nano-indentation, microindentation, miniature testing, heat treatment

OPEN ACCESS

Edited by:
Liqiang Wang,
Shanghai Jiao Tong University, China

Reviewed by:
Jose Eduardo Spinelli,
Federal University of São Carlos, Brazil
Lei Wang,
Xi'an University of Technology, China

****Correspondence:***
Daniel Röhrens
d.roehrens@access-technology.de

Specialty section:
This article was submitted to Structural Materials a section of the journal Frontiers in Materials

Received: *30 May 2020*
Accepted: *27 August 2020*
Published: *07 October 2020*

Citation:
Röhrens D, Navaeilavasani N, Stryzhyboroda O, Swientek F, Pavlov P, Meister D, Genau A and Hecht U (2020) Microstructure and Mechanical Properties of BCC-FCC Eutectics in Ternary, Quaternary and Quinary Alloys From the Al-Co-Cr-Fe-Ni System. Front. Mater. 7:567793. doi: 10.3389/fmats.2020.567793

INTRODUCTION

The intermetallic compound NiAl has long been proposed as a potential alloy for high temperature structural applications due to its high melting-point, good thermal conductivity and excellent corrosion resistance (Miracle, 1993; Noebe et al., 1993; Liu, 1995). Because of the relatively low density (5.7 g/cm^3) it was especially considered for lightweight applications (Bei and George, 2005). Resulting from a high degree of order in the crystal structure and corresponding limitations in slip transfer, NiAl suffers from low room temperature ductility and low fracture toughness. This

TABLE 1 | Alloy designation and composition of the samples as measured by energy dispersive spectroscopy.

Alloy designation and content, at%	Ternary $Ni_{48}Fe_{34}Al_{18}$	Quaternary $Ni_{44}Fe_{20}Cr_{20}Al_{16}$	Quinary $Ni_{34.4}Fe_{16.4}Co_{16.4}Cr_{16.4}Al_{16.4}$
Ni	47.2	43.4	34.1
Fe	33.9	20.4	15.5
Al	18.9	15.7	15.8
Cr	—	20.5	17.0
Co	—	—	17.5

drawback is further complemented by low strength and creep resistance at higher temperatures (>600 °C). Numerous approaches have been proposed in order to improve the mechanical properties of NiAl (Shang et al., 2012; Hu et al., 2013; Wang et al., 2014; Wang et al., 2019; Wang et al., 2017). For example, alloying with refractory metals such as Cr, Mo, Re, and V produced binary BCC-B2 eutectic alloys with improved toughness and creep strength (Misra et al., 1998; Bei and George, 2005). Another successful approach by Misra and Gibala involved the addition of large amounts of iron to produce BCC-B2/FCC eutectic alloys with much improved room temperature ductility (Misra and Gibala, 1997). The possible tailoring of microstructure and interfacial properties with the target of promoting slip transfer and ductility was further advanced by investigating directionally solidified $Ni_{50}Fe_{30}Al_{20}$ (Misra and Gibala, 1999). The authors studied slip transfer across the phase boundaries and could identify several compatible slip systems, given the Kurdjumow–Sachs orientation relationship (Kurdjumow and Sachs, 1930) between the BCC and FCC lamellae (Misra and Gibala, 1999). In particular, they found that the interphase slip transfer is similar to the transfer across grain boundaries, and as a result, the active slip system can be predicted by utilizing criteria that had been proposed for grain boundaries (Shen et al., 1988).

The idea of creating a eutectic microstructure with improved ductility and an increasing number of constituents was advanced further by Jin et al. (2019). By the addition of Cr to a Ni-Fe-Al alloy, for example, $Ni_{44}Fe_{20}Cr_{20}Al_{16}$, a eutectic microstructure composed of FCC and BCC-B2 was found and investigated. The authors reported good mechanical strength and ductility for this material, which they ascribed to the so-called high-entropy effect (Cantor et al., 2004; Chen et al., 2004). Many authors, including the study of Jin et al. postulate a thermodynamic explanation for the improved mechanical properties of those materials (Jin et al., 2019). However, there is currently an ongoing discussion about the fundamental reasoning behind and the validity of the high-entropy-effect, which is discussed in depth in an extensive review by Miracle and Senkov et al. (2017). Independent of the fundamental physical reasoning behind the effect, the class of multicomponent materials offers numerous possibilities for improving and tailoring alloys related to NiAl. This is especially true for eutectic materials with the nominal composition of $Ni_{34.4}Fe_{16.4}Co_{16.4}Cr_{16.4}Al_{16.4}$ (Lu et al., 2014; Gao et al., 2017), which turned out to be composed of FCC and BCC-B2 and was termed an eutectic high-entropy alloy (EHEA). A particularly good combination of high fracture strength and high ductility was reported to be retained even at temperatures of 700°C. The ratio of fracture stress to yield stress was shown to be about 1 order of magnitude larger for this EHEA than for NiAl-based alloys. Beneficial mechanical properties were both found and investigated by several groups (Gao et al., 2017; Nagase et al., 2017), including thermomechanical processing (Wani et al., 2016; Bhattacharjee et al., 2018). Summarizing, we found that FCC/BCC-B2 eutectics with lamellar microstructure were reported for ternary Al-Ni-Fe, quaternary Al-Ni-Fe-Cr, and quinary Al-Ni-Fe-Cr-Co alloys. The quaternary Co-free eutectic alloy could be preferable due to economic, societal, and political reasons (Tkaczyk et al., 2018).

The aim of this study was to take up the early work by Misra and Gibala (1997), Misra et al. (1998), Misra and Gibala (1999), and Misra et al. (2005) and compare the microstructure and properties of ternary FCC/BCC-B2 eutectics to the recent EHEAs reported by Lu et al. (2014), Gao et al. (2017), Jin et al. (2019). The main emphasis is given to the analysis of element partitioning between the two phases of the eutectic, the analysis of the nano- and micro-hardness, and a comparison of mechanical properties determined by three-point bending on as-cast and heat treated specimens.

EXPERIMENTAL METHODS

Sample Preparation

Specimens were produced using a commercial arc-melting setup (AM 500, Edmund Bühler GmbH, Germany) equipped with a suction casting unit. The furnace operates under argon atmosphere after having evacuated the chamber several times to ensure that the residual oxygen partial pressure is small. Samples were produced in 100 g batches from high-purity elements, being molted in the arc-melter and rapidly cooled down, either in the form of buttons or suction cast into cylindrical samples of Ø 10 mm × 150 mm. All samples were remolted three times to ensure chemical homogeneity. The overall chemical composition of the samples produced for this study is given in **Table 1** in at%.

We found that the composition of the ternary eutectic was slightly different from that of $Ni_{50}Fe_{30}Al_{20}$ given by Misra and Gibala (1999). According to our observations, the composition given in Misra's study is slightly off-eutectic and yields BCC-B2 dendrites as a primary phase. For the composition listed in **Table 1** we were able to avoid primary phases and achieve a two-phase FCC/BCC-B2 eutectic microstructure.

The specimens were analyzed in the as-cast state, and in addition, directional solidification at low growth velocity was

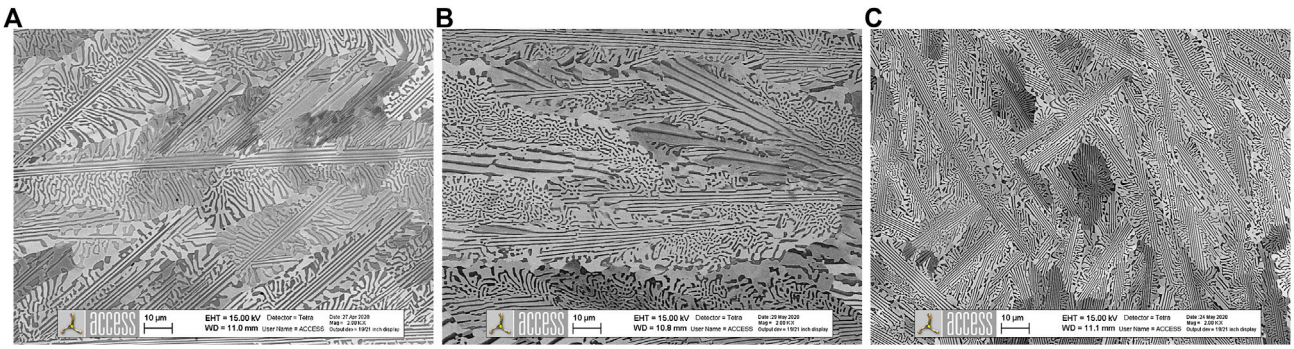

FIGURE 1 | Scanning electron microscopy backscatter-electron micrographs in 2000 X magnification of polished cross sections of as-cast arc-melted cylindrical samples of the $Ni_{48}Fe_{34}Al_{18}$ **(A)**, $Ni_{44}Fe_{20}Cr_{20}Al_{16}$ **(B)**, and $Ni_{34.4}Fe_{16.4}Co_{16.4}Cr_{16.4}Al_{16.4}$ alloys **(C)**.

carried out on the suction cast rods, in order to achieve planar coupled growth and provide equilibrium data about the phase composition. As-cast samples from the $Ni_{44}Fe_{20}Cr_{20}Al_{16}$ and $Ni_{34.4}Fe_{16.4}Co_{16.4}Cr_{16.4}Al_{16.4}$ eutectic alloys were further subjected to different annealing treatments which were carried out in a horizontal tube furnace under an argon (Ar 5.0) atmosphere at 750°C for 24 h and at 950°C for 15 h, respectively.

Directional solidification was carried out in a vertical Bridgman–Stockbarger furnace. This furnace features a heating zone on the top and a liquid metal cooling zone on the bottom, separated from one another by an isolation zone (baffle). The furnace operates under a protective argon (Ar 4.8) atmosphere. The setup was described in another article in more detail (Drevermann et al., 2004). For this study, the samples measuring Ø 8 mm × 150 mm were placed in an alumina tube, directionally molted over about 2/3rd of their length, and subsequently solidified at a velocity of 5 μm/sec over a length of 40 mm. The heater temperatures were set to 1,600°C. Directional solidification was finished by a quenching operation, achieved by a rapid, pneumatically driven movement of the cooler over the sample. The directionally solidified samples were cut along longitudinal and transverse section planes for further analysis. Phase composition measurements were performed on longitudinal sections close to the quenched solidification front.

Electron Microscopy, Energy Dispersive Spectroscopy, and Electron Backscatter Diffraction

The three alloys were analyzed by scanning electron microscopy (SEM) using ZEISS Gemini LEO 1550 and ZEISS Gemini Ultra 55 microscopes equipped with detectors for energy-dispersive spectroscopy (EDS) and electron backscatter diffraction (EBSD), that is, X-MaxN 150 and HKL Nordlys, respectively, being controlled and operated by INCA-software (Oxford Instruments). Sample preparation included conventional embedding, grinding, and polishing steps, with a final step of vibratory polishing (Vibromet, Buehler). EDS measurements were conducted in point-, line-scan, and area modes at 15 kV acceleration voltage and a working distance of 10 mm. EDS line scans were conducted perpendicular to the lamellar microstructure for all three alloys to determine the chemical composition of the individual phases in the two-phase eutectic. Crystallographic information was obtained using EBSD maps. Additionally, phase fractions were determined from backscatter-SEM images (1,024 pixels × 768 pixels) in 2,000× magnification using the open-source software ImageJ (Schneider et al., 2012). For each of the as-cast alloys, three individual pictures were analyzed.

Indentation Experiments

Micro-indentation

Micro-indentation experiments were carried out in the indentation MHT3 from Anton Paar GmbH, Germany. The system allows for a continuous measurement of the penetration depth of a defined indentation tip as a function of the loading force (load–depth profiles). Positioning of the imprints on the sample surface is facilitated by an in-built light microscope. Micro-indentation measurements were carried out using a diamond indentation tip in Vickers geometry, which had been calibrated before to determine the area function. Load-depth curves were recorded in the load-controlled mode using 1,000 mN maximum load, a 2,000 mN/min loading and unloading rate, and a 10-sec pause on maximum load. Indents were placed in the form of a predefined matrix across the surface. The distance between each individual indent was 75 μm, while the diagonal for the imprint under these conditions was about 25 μm. The Oliver–Pharr algorithm was applied to determine the microhardness and Young's modulus from the unloading characteristics. The selected set of parameters

TABLE 2 | Phase fractions in as-cast samples from image analysis and electron backscatter diffraction (EBSD) mapping, in area%.

Phase fraction	Image analysis $Ni_{48}Fe_{34}Al_{18}$	EBSD map $Ni_{48}Fe_{34}Al_{18}$	Image analysis $Ni_{44}Fe_{20}Cr_{20}Al_{16}$	Image analysis $Ni_{34.4}Fe_{16.4}Co_{16.4}Cr_{16.4}Al_{16.4}$
FCC	60	59.2	68	70
BCC-B2	40	40.8	32	30

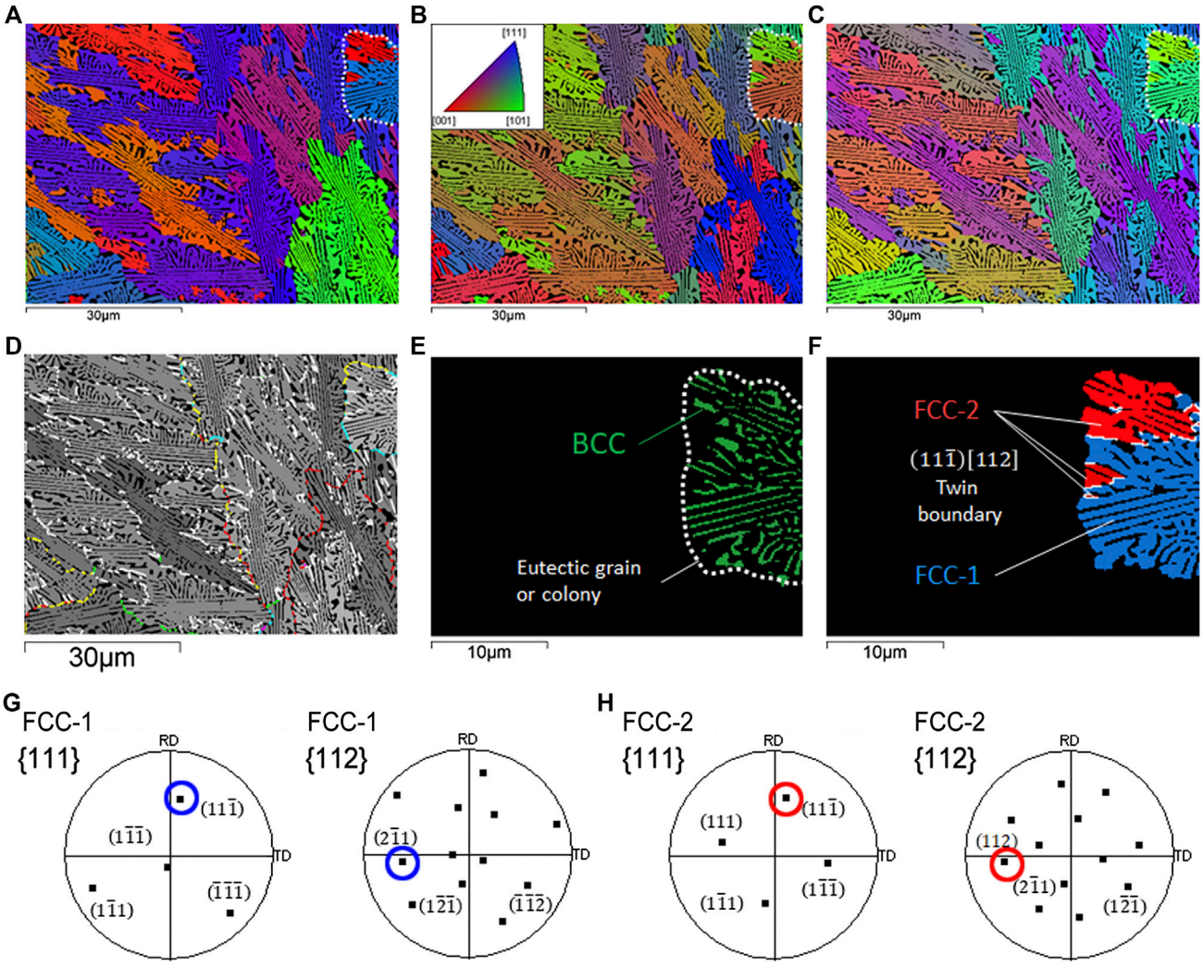

FIGURE 2 | FCC twins in the as-cast quinary eutectic alloy $Ni_{34.4}Fe_{16.4}Co_{16.4}Cr_{16.4}Al_{16.4}$ based on electron backscatter diffraction mapping results: **(A–C)** inverse pole figure coloring of the FCC orientation, **(D)** grain boundaries (colored lines) and twin boundaries (white lines) in the mapping region, **(E, F)** zoom-in view into one eutectic grain which features a single BCC orientation but two distinct FCC orientations separated by $(11\bar{1})[112]$ twin boundaries, **(G, H)** pole figures for {111} and {112} plane families corresponding to FCC-1 and FCC-2, respectively. The common planes/directions are marked with circles.

ensured a sufficiently large size of the imprint encompassing several lamellae, while at the same time being small enough to capture individual grain properties. Additionally, the selected load is in a range for optimal signal-to-noise characteristics in the raw data.

Nano-Indentation

Nano-indentation measurements twere carried out by Anton Paar GmbH, Germany, on a nanohardness tester (NHT). As with the micro-indentation system, a continuous measurement of penetration depth as a function of an applied axial load was recorded. All nano-indentation experiments were carried out using a diamond indentation tip in Berkovich geometry (cube corner). The indentations followed a predefined 11 × 11 matrix across a polished cross section of the specific samples, set up as lines of equi-distant points with a 3-μm distance, which ensures a sufficient spacing so that none of the neighboring indentations are affected by localized strain. Load–depth curves were recorded in load-controlled procedures using 1.0 mN maximum load, a 2.0-mN/min loading and unloading rate, and a 10-sec pause on maximum load. The Oliver–Pharr algorithm was used to determine the nano-hardness and Young's modulus from the unloading characteristics. Surface detection limits were set to 0.1 mN for each measurement. The resulting imprints were comparatively small with around 60 nm depth and 300 nm diagonal width. Most of them were well inside specific phases (lamellae), which allowed for the collection of phase specific indentation curves and properties.

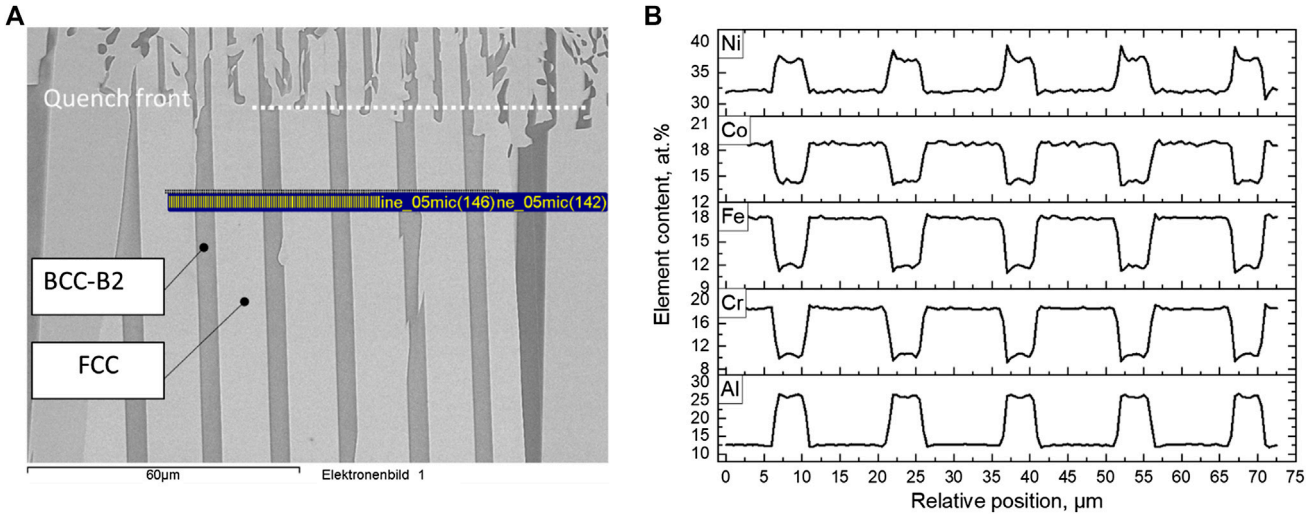

FIGURE 3 | Energy dispersive spectroscopy line scan and measured element partitioning between the two phases of the eutectic exemplarily shown for the quinary alloy $Ni_{34.4}Fe_{16.4}Co_{16.4}Cr_{16.4}Al_{16.4}$ at the quenched front of the directional solidified sample **(A)**. The composition profiles displayed in **(B)** show that both phases are multicomponent: while the BCC-B2 phase is rich in Ni and Al, the FCC phase is rich in Fe and Cr. Co partitions to the FCC phase.

Three-Point Bending Tests

Three-point bending tests were conducted on $Ni_{48}Fe_{34}Al_{18}$, $Ni_{44}Fe_{20}Cr_{20}Al_{16}$, and $Ni_{34.4}Fe_{16.4}Co_{16.4}Cr_{16.4}Al_{16.4}$ specimens using a micromechanical stage SEMtester 1000 EBSD instrument (MTI Instruments Inc., United States). Rectangular specimens measuring 30.0 mm × 5.0 mm× 1.6 mm were cut from suction cast bars and by wire erosion cutting and tested in the as-cast state. Samples from the $Ni_{44}Fe_{20}Cr_{20}Al_{16}$ and $Ni_{34.4}Fe_{16.4}Co_{16.4}Cr_{16.4}Al_{16.4}$ alloys were also tested in heat-treated conditions, for example, at 750°C/24 h and at 950°C/15 h, respectively. Flexural stress-strain curves were calculated following the procedures outlined in the ASTM testing standard (Raheem, 2019).

TABLE 3 | Quantitative energy dispersive spectroscopy-analysis of directionally solidified samples close to the solidification front.

	Eutectic (at%)	BCC-B2		FCC-A1	
		(at%)	Std. dev.	(at%)	Std. dev.
$Ni_{48}Fe_{34}Al_{18}$					
Al	18.9	25.5	0.4	14.8	0.4
Fe	33.9	26.6	0.5	39.7	0.4
Ni	47.2	47.9	0.3	45.5	0.2
$Ni_{44}Fe_{20}Cr_{20}Al_{16}$					
Al	15.7	25.8	0.3	10.8	0.2
Cr	20.5	12.2	0.8	24.4	0.2
Fe	20.4	13.5	0.4	23.7	0.2
Ni	43.4	48.5	1.0	41.1	0.2
$Ni_{34.4}Fe_{16.4}Co_{16.4}Cr_{16.4}Al_{16.4}$					
Al	15.8	26.1	0.4	12.4	0.2
Cr	17.0	10.4	0.5	18.6	0.2
Fe	15.5	11.8	0.3	18.0	0.2
Co	17.5	14.4	0.2	18.8	0.2
Ni	34.1	37.4	0.7	32.1	0.2

RESULTS AND DISCUSSION

Microstructure

As-cast samples from arc-melting and suction casting were prepared metallographically and subsequently analyzed by SEM according to the information given in chapter 2. All samples in the as-cast state showed a two-phase lamellar eutectic microstructure, low porosity, and no cracks. The as-cast microstructure is shown in **Figure 1**. The eutectic has a clear cellular/"dendritic" appearance with a sharply defined lamellar morphology in the trunk center and radially branching lamellae toward the cell sides. The FCC phase (bright) is the majority phase, while the BCC-B2 phase (dark) is the minority phase. While the three alloys look similar, the microstructure is finer in the $Ni_{44}Fe_{20}Cr_{20}Al_{16}$ and $Ni_{34.4}Fe_{16.4}Co_{16.4}Cr_{16.4}Al_{16.4}$ samples, which exhibit smaller lamellar spacings in the trunc region, and a higher fraction of the FCC phase. Lamellar spacings were estimated to be in the range around 1.2–1.4 µm in the $Ni_{44}Fe_{20}Cr_{20}Al_{16}$ and $Ni_{34.4}Fe_{16.4}Co_{16.4}Cr_{16.4}Al_{16.4}$ samples, while being slightly larger in the $Ni_{48}Fe_{34}Al_{18}$ sample, for example, 1.4–2.1 µm, due to faster diffusion owing to higher liquidus and solidus temperatures. The spacing estimation was done by the line intercept method and limited to the core region of eutectic colonies, where the lamellar structure is prominent and clear.

Quantitative phase analysis using the open-source software ImageJ was used to measure phase fractions. For the $Ni_{48}Fe_{34}Al_{18}$ alloy, the phase fractions were also verified by EBSD mapping. The results are listed in **Table 2**. The $Ni_{48}Fe_{34}Al_{18}$ sample consists of roughly 60% FCC, while both the $Ni_{44}Fe_{20}Cr_{20}Al_{16}$ and $Ni_{34.4}Fe_{16.4}Co_{16.4}Cr_{16.4}Al_{16.4}$ alloys show an increase in the FCC fraction to about 70%.

In all samples, we observed that the FCC phase inside the eutectic grains or colonies, which were formed as a result of

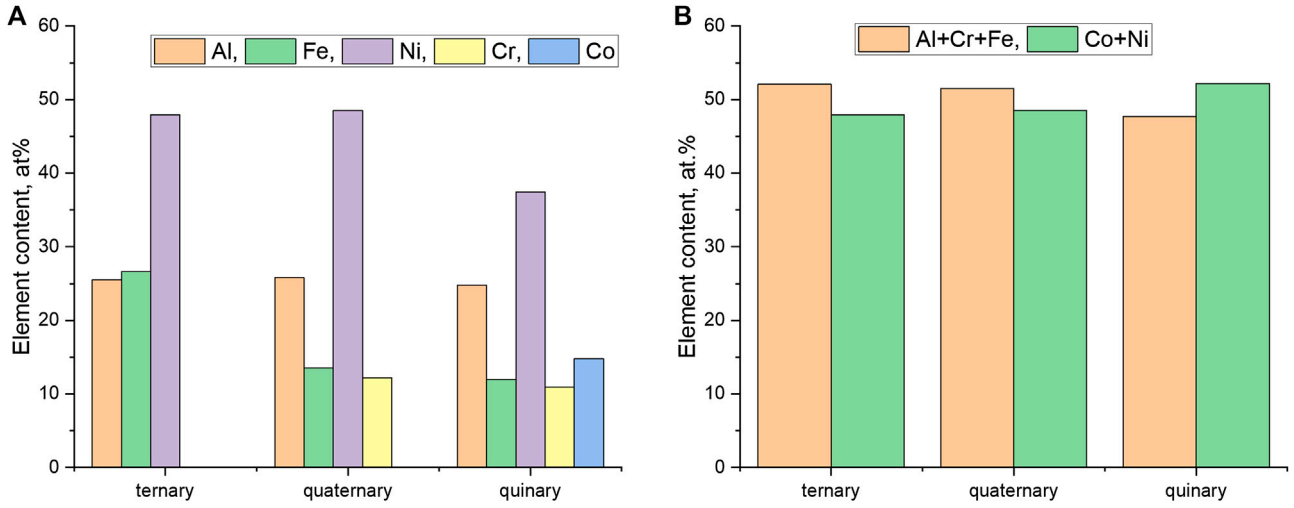

FIGURE 4 | Graphical visualization of the compositional data of the BCC-B2 phase for all three alloys given in **Table 3 (**A**)** and grouping of the elements according to two separate crystallographic sites in the BCC-B2 phase **(B)**.

Mullins–Sekerka instabilities (Plapp and Karma, 2002) in large columnar eutectic grains, displays growth twins. Twinning of the FCC phase is illustrated in **Figure 2** for the as-cast quinary eutectic $Ni_{34.4}Fe_{16.4}Co_{16.4}Cr_{16.4}Al_{16.4}$ based on EBSD mapping results. The orientation of the FCC phase is shown using inverse pole figure coloring for the normal direction (**Figure 2A**), the rolling direction (**Figure 2B**) and the transverse direction (**Figure 2C**). In the upper right corner of these inverse pole figure maps, one grain is outlined with a dotted white line. As seen in **Figure 2D**, the grain is bounded by yellow and turquoise

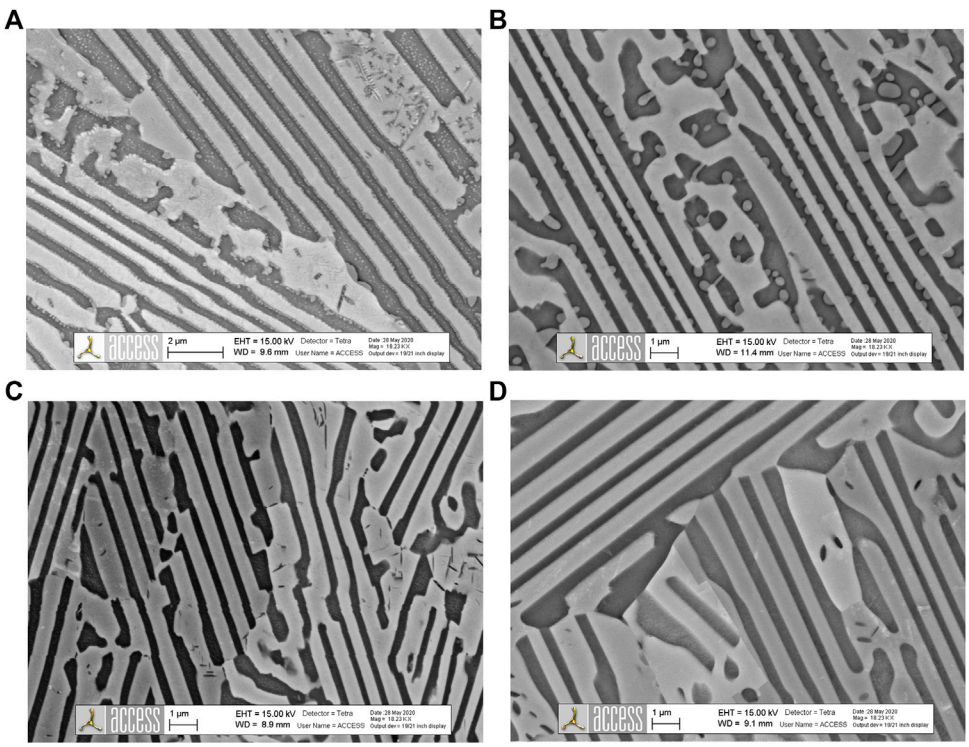

FIGURE 5 | Scanning Electron Microscopy micrographs of samples of the $Ni_{44}Fe_{20}Cr_{20}Al_{16}$ alloy after treatment at 750°C **(A)** and after 950°C **(B)**, the $Ni_{34.4}Fe_{16.4}Co_{16.4}Cr_{16.4}Al_{16.4}$ samples after 750°C **(C)** and after 950°C **(D)**.

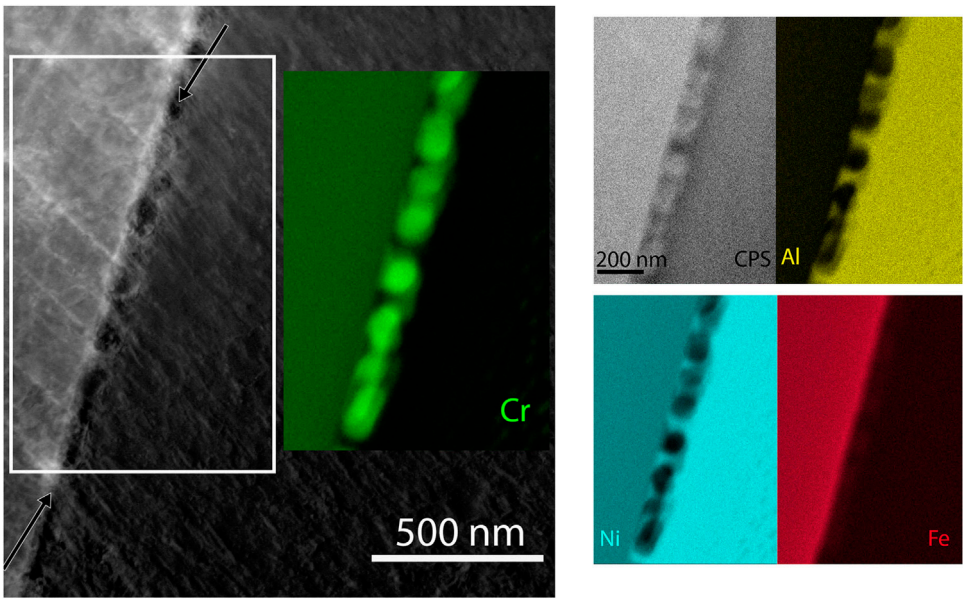

FIGURE 6 | Scanning transmission electron microscopy image in high-angle annular dark-field mode and transmission electron microscopy-energy dispersive spectroscopy map of a characteristic interface region between the FCC and BCC-B2 lamellae of a sample of the directionally solidified $Ni_{44}Fe_{20}Cr_{20}Al_{16}$ alloy.

borders toward neighboring grains, but internally it contains distinct regions separated by white boundaries. In fact, the white boundaries are twin boundaries. A zoom-in view of the FCC twin boundaries in this grain is provided in **Figure 2F**, while **Figure 2E** shows that a single BCC orientation prevails in the eutectic grain. We identified the twinning plane and direction between the two regions FCC-1 and FCC-2 to be $(11\bar{1})[112]$. The corresponding pole figures for {111} and {112} plane families are presented in **Figure 2G** for FCC-1 and in **Figure 2H** for FCC-2. The twinning system is characteristic for FCC growth twins. We observed a remarkably high amount of twin boundaries in the mapping region (compare **Figure 2D**). More details about twinning in this EHEA will be presented in an upcoming publication.

Directional Solidification

Directionally solidified samples with planar growth front and coupled eutectic growth patterns with large lamellae size were used to accurately measure the phase composition using EDS line scans across several lamellae. A step size of 0.5 µm was used. EDS analysis has been shown previously to be an adequate method for elemental quantification (Newbury and Ritchie, 2013). Line scans have been conducted a few below the quenched front in the directionally solidified area. We present the data from a single line scan for each of the three alloys, containing about 150 single-point spectra. **Figure 3** exemplarily shows a line scan and the measured element distribution across the FCC and BCC-B2 lamellae from the alloy $Ni_{34.4}Fe_{16.4}Co_{16.4}Cr_{16.4}Al_{16.4}$. **Table 3** contains the phase composition data for all three investigated alloys measured by the same procedure.

The ordered BCC-B2 phase in all three alloys is derived from the ordered compound NiAl, which is known to crystallize in a CsCl-type structure (space-group 221, Pearson symbol cP2). From the data presented in **Table 3** and **Figure 4** it is deduced that an approximate composition of $(Ni, Co)_{50}$ $(Al, Cr, Fe)_{50}$ is valid for the BCC-B2 phase, with Co occupying Ni sites, while Fe and Cr prefer the Al-sites. If elements Al, Cr, and Fe are grouped together and a second group of Ni, and Co is established, the summation of the data in **Table 3** leads to an equally distributed elemental composition within the two groups (see **Figure 4B**). These findings are consistent with literature data: Duncan et al. used atom probe field ion microscopy to show Fe preferentially occupying Al sites in NiAl (Duncan et al., 1994). Other studies found Cr clearly preferring Al sites (Medvedeva et al., 1998), while Co is found on the Ni sites, which is to be expected from the chemical similarity of the two elements (Li et al., 2016). It has to be noted that all these studies were conducted for very low concentrations of the substituting elements (Jones, 2003). This consideration has been conducted only for the ordered BCC-B2 phase since in the FCC phase all the atoms share all sites statistically.

To our knowledge, single-phase specific compositional data for the $Ni_{48}Fe_{34}Al_{18}$ and $Ni_{44}Fe_{20}Cr_{20}Al_{16}$ eutectics have not been published so far. For the $Ni_{34.4}Fe_{16.4}Co_{16.4}Cr_{16.4}Al_{16.4}$ alloy, Gao et al. determined elemental distributions for single phase lamellae with atom probe tomography that deviate significantly from our results (Gao et al., 2017). We believe this deviation can be attributed to both the atom probe tomography method of quantification in Gaos's study which is sensitive to local fluctuations and a different method of preparation of the specimens. Wang et al. published phase-specific compositional data obtained by SEM-EDS for the eutectic $Ni_{34.4}Fe_{16.4}Co_{16.4}Cr_{16.4}Al_{16.4}$ which exhibits similar results to this study (Wang et al., 2020).

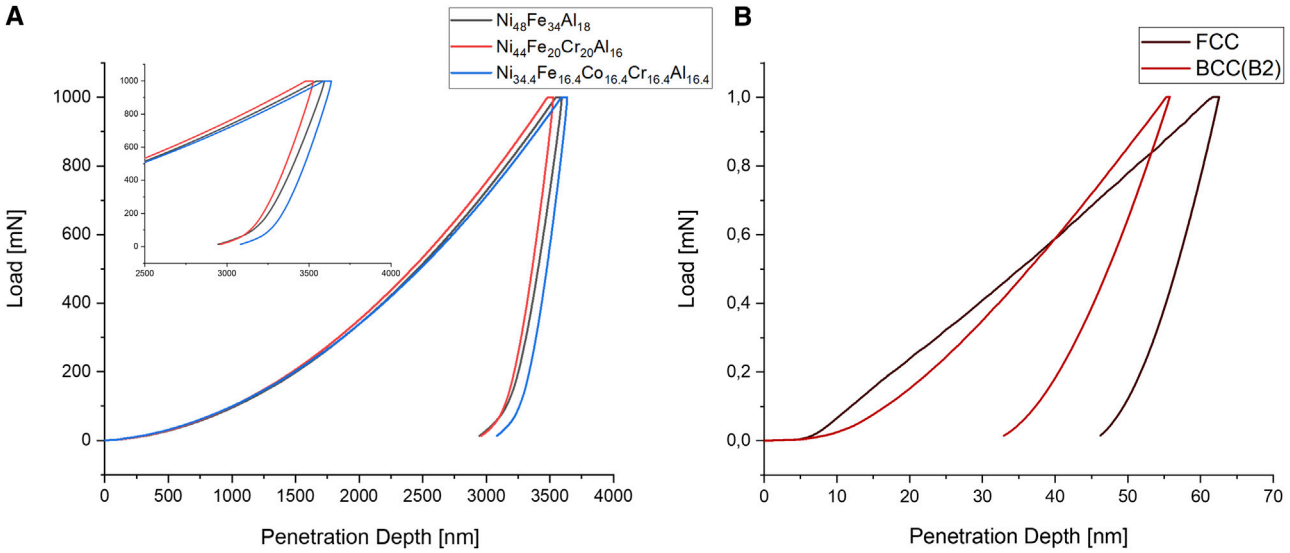

FIGURE 7 | Mean load-depth profiles of the three alloys from micro-indentation experiments **(A)** and mean load-depth profiles of nano-indentation probing of the individual phases of the $Ni_{44}Fe_{20}Cr_{20}Al_{16}$ alloy **(B)**.

As can be deduced from these results, the BCC-B2 phase is rich in Al and Ni, while the FCC phase is rich in Fe, and where applicable Cr, and Co. While this finding holds true for all the analyzed regions in this study, we want to emphasize that always all the elements are present in each individual phase in significant amounts (>10 at%), which is an important finding in regard to the discussion of a potential high-entropy effect.

Isothermal Heat Treatment

In order to assess the potential for altering the mechanical properties of the eutectic alloys, two different heat treatments were conducted for the $Ni_{44}Fe_{20}Cr_{20}Al_{16}$ and $Ni_{34.4}Fe_{16.4}Co_{16.4}Cr_{16.4}Al_{16.4}$ samples, that is, 750 °C for 24 h and 950 °C for 15 h. In this case, the $Ni_{48}Fe_{34}Al_{18}$ alloy was not included. In the SEM analysis of the heat-treated $Ni_{44}Fe_{20}Cr_{20}Al_{16}$ samples we observed needle-like precipitation in the FCC phase and a new Cr-rich phase. The phase boundaries appear fully and densely covered with small particles of this new phase. As shown in **Figure 5A** for samples heat-treated at 750°C and **Figure 5B** for samples heat-treated at 950°C the thickness of this layer increases with temperature and time, a result of coarsening. Along with coarsening at 950°C, the Cr-rich particle layer no longer fully covers the interface. The nature of the Cr-rich phase could not be identified unambiguously, but we expect it to be a Cr-rich BCC-A2 phase. A potential σ-phase could be excluded by EBSD. Interestingly, as revealed by transmission electron microscopy analysis, we found that this Cr-rich layer was already present for an as-cast sample of the $Ni_{44}Fe_{20}Cr_{20}Al_{16}$ alloy. This is shown in **Figure 6**. We attribute this behavior to the relatively large Cr content of the $Ni_{44}Fe_{20}Cr_{20}Al_{16}$ eutectic alloy, which is 20.5 vs. 17.0 at% for the $Ni_{34.4}Fe_{16.4}Co_{16.4}Cr_{16.4}Al_{16.4}$. In contrast, the $Ni_{34.4}Fe_{16.4}Co_{16.4}Cr_{16.4}Al_{16.4}$ alloy did not exhibit a Cr-rich layer at the lamellar interface after the same heat treatments at 750°C (**Figure 5C**) and 950°C (**Figure 5D**). We observed needle-like precipitates in the FCC-phase of the $Ni_{34.4}Fe_{16.4}Co_{16.4}Cr_{16.4}Al_{16.4}$ samples, which also showed a tendency toward coarsening at 950°C.

In summary, applying the afore-mentioned heat treatments to the $Ni_{44}Fe_{20}Cr_{20}Al_{16}$ and $Ni_{34.4}Fe_{16.4}Co_{16.4}Cr_{16.4}Al_{16.4}$ samples revealed significant differences between the two alloys, which will impact the mechanical behavior in the three-point bending experiments shown in *Three-Point Bending Experiments*. The appearance and coarsening of the Cr-rich layer that covers the lamellar interfaces of the $Ni_{44}Fe_{20}Cr_{20}Al_{16}$ samples demonstrated the necessity for a heat treatment that is adapted to this system, and the 950°C treatment may constitute a starting point for further research.

TABLE 4 | Instrumented hardness (H_{IT}) and Young's modulus (E_{IT}) for the three alloys as determined by micro-indentation experiments and for the individual phases of the Ni44Fe20Cr20Al16 alloy as determined by nano-indentation.

	H_{IT} (MPa)	Std. dev.	E_{IT} (GPa)	Std. dev	N
Micro-indentation alloy					
$Ni_{48}Fe_{34}Al_{18}$	3472.1	67.9	158.0	6.7	52
$Ni_{44}Fe_{20}Cr_{20}Al_{16}$	3537.5	93.7	188.1	7.6	46
$Ni_{34.4}Fe_{16.4}Co_{16.4}Cr_{16.4}Al_{16.4}$	3310.1	71.2	185.9	8.5	44
Nano-indentation phase					
$Ni_{44}Fe_{20}Cr_{20}Al_{16}$-FCC	4721.9	215.5	190.1	9.1	49
$Ni_{44}Fe_{20}Cr_{20}Al_{16}$-BCC-B2	6016.8	472.6	144.4	10.2	30

Indentation

Selected samples were subjected to indentation experiments using the depth-sensing indentation technique, as outlined in *Indentation Experiments*. Thereby, synchronously load and depth were recorded and plotted as a load–depth profile. With a known indenter shape, the specimen's hardness and Young's

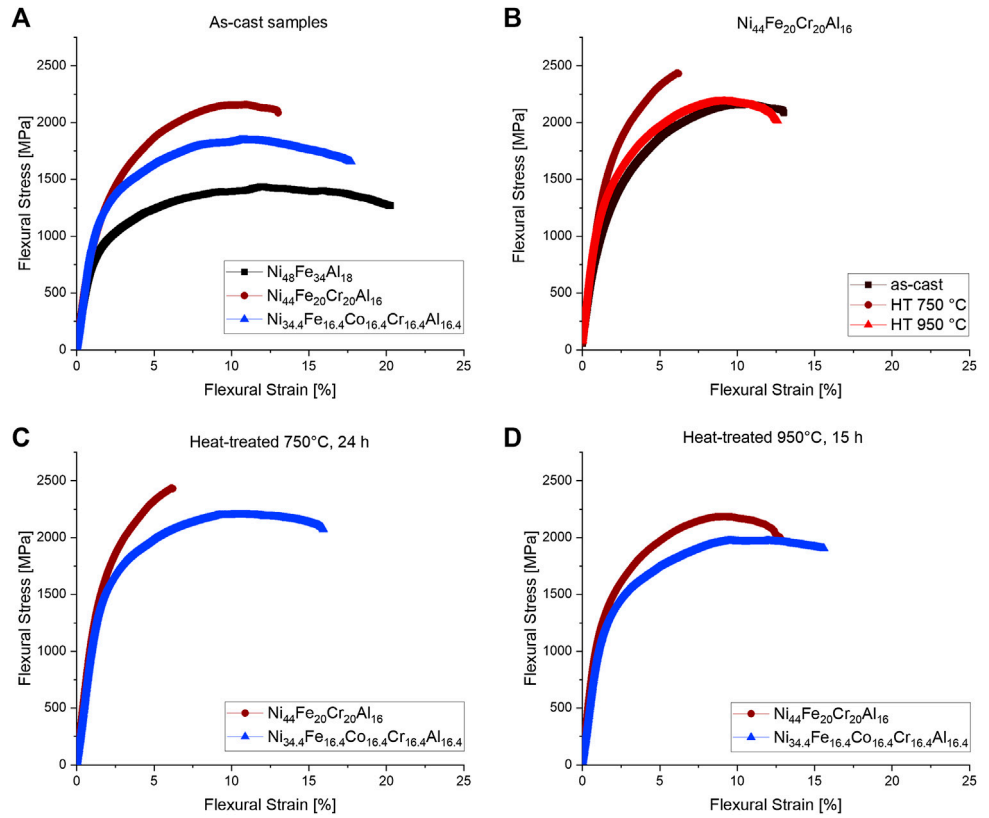

FIGURE 8 | Comparison of results from three point bending experiments of as-cast alloys **(A)**, the $Ni_{44}Fe_{20}Cr_{20}Al_{16}$ alloy after different treatments **(B)**, both the $Ni_{44}Fe_{20}Cr_{20}Al_{16}$ and $Ni_{34.4}Fe_{16.4}Co_{16.4}Cr_{16.4}Al_{16.4}$ alloys after heat treatment at 750 °C for 24 h **(C)**, and after heat treatment at 950 °C for 15 h **(D)**.

modulus were calculated following to the procedure laid out by Oliver and Pharr (1992). The method relies on fitting a power law to the unloading part of the load–depth profile and works well for the comparison of specimens.

Micro-Indentation

The aim of these experiments was the determination of Young's modulus and microhardness for as-cast eutectic samples. The size of the indentation tip always covered several lamellae within a grain. Around 50 individual indents were placed on eutectic grains to ensure sufficient statistics. As can be seen from the data presented in **Table 4** and **Figure 7A**, both the $Ni_{44}Fe_{20}Cr_{20}Al_{16}$ and $Ni_{34.4}Fe_{16.4}Co_{16.4}Cr_{16.4}Al_{16.4}$ alloys showed nearly identical elastic behavior as demonstrated by the instrumented Young modulus. The $Ni_{48}Fe_{34}Al_{18}$ system was found to exhibit a significantly smaller elastic constant. As for the microhardness, all three samples led to similar results, while the $Ni_{44}Fe_{20}Cr_{20}Al_{16}$ alloy was observed to show the highest values, closely followed by the $Ni_{48}Fe_{34}Al_{18}$ within one standard deviation. For the $Ni_{34.4}Fe_{16.4}Co_{16.4}Cr_{16.4}Al_{16.4}$ sample, a statistically significantly smaller hardness was recorded. The local response of the materials did not vary significantly as is demonstrated by the relatively low standard deviations in **Table 4**. In a separate set of experiments, numerous indentations have been placed selectively in different grains. The analysis of that experiment did not give any indication of orientation anisotropy.

The microhardness values for all eutectics in the as-cast state range around 350 H_v, which compares well to the hardness values reported for $Al_xCoCrFeNi$ alloys by Wang et al. (2012), for x ranging from 0.65 to 0.75. This is in agreement with the dual-phase nature of the material which for the given molar ratio x, contains about 60–70% FCC phase.

Nano-Indentation

In contrast to the micro-indentation experiments, the aim of the nano-indentation study was the determination of single-phase properties for the individual FCC and BCC-B2 lamellae. In this part of the study, we focused exclusively on the $Ni_{44}Fe_{20}Cr_{20}Al_{16}$ alloy as a representative system. To ensure a fully single-phase result, we conducted these experiments through cross sections of directionally solidified samples for which lamellar spacings of several micrometers were obtained, much larger than for the as-cast samples. The indentations were positioned so that the actual indent was probing the lamellae in growth direction. Because of the high symmetry of the two phases, we did not expect strong anisotropy of the phase-specific mechanical properties. Further investigation into the anisotropic behavior is beyond the scope of this study, but may be conducted in future research.

The indents were positioned in a quadratic 11 × 11 matrix of equidistant points across the samples, which ensured that five lamellae of each phase were covered within that area. The distance of each point is 3 μm both in the *x* and *y* directions, which is sufficiently large compared to the approximate 0.3–0.5 μm diameter of the indents. This ensures that the mechanical properties determined by the indentation are not influenced by the plastic deformation of neighboring indentations.

The resulting 121 load-controlled single measurements were transformed into load–depth curves and subsequently grouped into two sets of phase-specific measurements according to their position on the microscopic image and the mechanical data. Since the BCC-B2 phase is significantly less deformable than the FCC phase, the phases were identified unambiguously. Only a small number of measurements could not be clearly assigned to one of the two phases, probably due to the proximity to a phase boundary, and they were subsequently removed from the dataset. The number of indentations in the FCC group vs. the BCC-B2 group matches roughly the phase fractions determined by image analysis and EBSD, so the phase assignment during nano-indentation analysis agrees with findings presented in previous chapters (see *Results and Discussion* and *Microstructure*). Each phase specific group of indentation curves was transformed into a mean-curve to visualize and represent the data concisely in **Figure 7B**. As expected, the FCC phase is more ductile, that is, leads to much deeper penetration depths for the same applied maximum load, and also shows an earlier onset of plastic deformation already in the loading curve. Despite the visual appearance, the two unloading curves are not perfectly parallel, which means that the elastic properties for both phases are significantly different. We determined the Young modulus of the ductile FCC phase is significantly larger than the corresponding value for the BCC-B2 phase. The experiments were so far not repeated for the other alloys as the focus of this part of the study was only on the acquisition and comparison of phase-specific data.

It has to be noted that the results for hardness from nano-indentation are not easily comparable to the corresponding results from micro-indentation. As is visible in **Table 4** the apparent hardness as of nano-indentation is significantly higher for both single phases than for the eutectic grains as obtained from micro-indentation. Both values can however not be compared directly, because of the indentation size effect, a phenomenon that is well known and described in the literature (Qian et al., 2005). The magnitude of the indentation size effect is dependent on the maximum load applied and thus most pronounced for nano-indentation experiments. The results from both nano- and micro-indentation are presented in **Figure 7** and summarized in **Table 4**.

Three Point Bending Experiments

In order to investigate the influence of composition and potentially reveal high-entropy effects on the mechanical properties of the alloys, we conducted a set of deformation experiments in three-point bending configuration. The results are shown in **Figure 8** and summarized in **Table 5**.

As is shown in **Figure 8A**, the $Ni_{48}Fe_{34}Al_{18}$ sample was found to be less strong and more ductile than the $Ni_{44}Fe_{20}Cr_{20}Al_{16}$ and $Ni_{34.4}Fe_{16.4}Co_{16.4}Cr_{16.4}Al_{16.4}$ samples in the as-cast state. The coarser lamellar structure of the $Ni_{48}Fe_{34}Al_{18}$ alloy contributes to this behavior. Additionally, we never observed any kind of nanometer-sized precipitation for the $Ni_{48}Fe_{34}Al_{18}$ alloy as opposed to the $Ni_{44}Fe_{20}Cr_{20}Al_{16}$ samples, which also may influence the mechanical response and higher ductility. In fact, during the bending experiments, only the $Ni_{48}Fe_{34}Al_{18}$ samples did not fracture during the measurements, as opposed to the other two samples for which all of the specimens fractured at some earlier point. The maximum flexural strain of 23% for the as-cast $Ni_{48}Fe_{34}Al_{18}$ alloy given in **Table 5** represents the limit of the measurement setup. In agreement with micro-indentation data, the $Ni_{48}Fe_{34}Al_{18}$ system also shows the lowest elastic constant. Remarkably, upon introduction of Cr and Co, the $Ni_{44}Fe_{20}Cr_{20}Al_{16}$ and $Ni_{34.4}Fe_{16.4}Co_{16.4}Cr_{16.4}Al_{16.4}$ eutectic samples showed a higher Young modulus, yield, and ultimate strength, and most importantly a more pronounced work hardening, while all these effects were found to be in a similar range for the $Ni_{44}Fe_{20}Cr_{20}Al_{16}$ and $Ni_{34.4}Fe_{16.4}Co_{16.4}Cr_{16.4}Al_{16.4}$ samples. The work hardening may indeed relate to the high-entropy effect. This finding is even more notable when viewed in the context of the results from quantitative phase analysis in which it was determined that the phase fractions expressed as ratio between FCC and the less ductile BCC-B2 phases went from roughly 60:40 for the $Ni_{48}Fe_{34}Al_{18}$ to roughly 70:30 for the $Ni_{44}Fe_{20}Cr_{20}Al_{16}$ and $Ni_{34.4}Fe_{16.4}Co_{16.4}Cr_{16.4}Al_{16.4}$ samples. The $Ni_{44}Fe_{20}Cr_{20}Al_{16}$

TABLE 5 | Summary of the mechanical data as obtained from three point bending experiments conducted on various bar samples of the three alloys.

	Young's Modulus (GPa)	Yield strength (MPa)	Ultimate strength (MPa)	Flexural strain at fracture (%)
$Ni_{48}Fe_{34}Al_{18}$				
As-cast	76	696	1,394	23.0
$Ni_{44}Fe_{20}Cr_{20}Al_{16}$				
As-cast	96	767	2,157	12.6
Heat-treated 750°C	114	1,181	2,431	6.2
Heat-treated 950°C	123	1,094	2,183	12.5
$Ni_{34.4}Fe_{16.4}Co_{16.4}Cr_{16.4}Al_{16.4}$				
As-cast	94	893	1,842	18.9
Heat-treated 750°C	105	1,291	2,199	16.1
Heat-treated 950°C	104	1,021	1,968	15.6

samples showed higher strength at the expense of ductility than the $Ni_{34.4}Fe_{16.4}Co_{16.4}Cr_{16.4}Al_{16.4}$ samples, which may relate to the presence of the layer of Cr-rich precipitates along the interfacial boundaries.

For the heat-treated samples, we recorded significant changes in the mechanical response as is to be expected considering the microstructural changes discussed in *Indentation*. This was most strongly observed in the $Ni_{44}Fe_{20}Cr_{20}Al_{16}$ alloy (see **Figures 8B,C**), which showed embrittlement after treatment at 750°C, that is, an increase in yield strength and UTS, and a flexural strain at fracture of only 6.2%, the lowest value in the series. We believe the presence of the layer of Cr-rich precipitates along the interfacial boundaries as shown in **Figure 5A** to be responsible for this effect. Upon heat treatment at 950°C, those precipitates were shown do undergo coarsening, leading to fewer but larger precipitates, and most of the phase boundaries were shown to be uncovered (see **Figure 5B**). This finding explains the recovery of the flexural strain while most of the strength is retained (see **Figures 8B,D**). Additionally, for all analyzed samples, a higher elastic constant was determined after heat treatment. The heat-treated samples of the $Ni_{34.4}Fe_{16.4}Co_{16.4}Cr_{16.4}Al_{16.4}$ alloy (see **Figures 8C,D**) behaved similarly in terms of Young's modulus, yield, and UTS points but were shown to be more ductile than the $Ni_{44}Fe_{20}Cr_{20}Al_{16}$ samples. The $Ni_{34.4}Fe_{16.4}Co_{16.4}Cr_{16.4}Al_{16.4}$ sample did not experience a loss of ductility after heat treatment at 750°C, which is consistent with the microstructural analysis (see **Figure 5C**). The increase in yield and ultimate strength for all the heat-treated samples in **Table 5** is related to precipitation hardening due to the formation of small crystallites, as depicted in **Figure 5**.

From these results, we conclude that an annealing heat treatment at 950°C for 6–15 h is a good range for both the $Ni_{44}Fe_{20}Cr_{20}Al_{16}$ and $Ni_{34.4}Fe_{16.4}Co_{16.4}Cr_{16.4}Al_{16.4}$ alloys. Yet, the microstructural findings suggest that care must be taken during thermal treatment in order to avoid detrimental formation of interfacial layers.

CONCLUSIONS

In this study, we investigated three eutectic alloys composed of FCC and BCC-B2 lamellae with ternary ($Ni_{48}Fe_{34}Al_{18}$), ($Ni_{34.4}Fe_{16.4}Co_{16.4}Cr_{16.4}Al_{16.4}$) composition. The main results are as follows:

- All three alloys exhibit a lamellar eutectic microstructure and similar morphology. They consist predominantly of an FCC phase and a smaller but significant fraction of a BCC-B2 phase. The phase fraction of FCC increases when moving $Ni_{34.4}Fe_{16.4}Co_{16.4}Cr_{16.4}Al_{16.4}$ alloy.
- Remarkably, all the elements that make up the three alloys are present in both of the phases, so indeed the $Ni_{44}Fe_{20}Cr_{20}Al_{16}$ and $Ni_{34.4}Fe_{16.4}Co_{16.4}Cr_{16.4}Al_{16.4}$ alloys may be regarded as high-entropy alloys.
- For all three alloys the FCC-phase contains more Fe, Cr, and Co respectively, while the BCC-B2 phase is rich in both Al and Ni, which demonstrates its relationship to the compound NiAl.
- Although it had the highest content of the BCC-B2 phase, the $Ni_{48}Fe_{34}Al_{18}$ alloy showed the least strength and the highest ductility while the effect of work hardening to flexural strength is limited.
- Additions of Cr and Co led to an increase in Young's modulus as measured by three-point bending. Additionally, a higher yield strength and ultimate strength values were recorded for the $Ni_{44}Fe_{20}Cr_{20}Al_{16}$ and $Ni_{34.4}Fe_{16.4}Co_{16.4}Cr_{16.4}Al_{16.4}$ eutectics than for the $Ni_{48}Fe_{34}Al_{18}$. Both alloys show significant work hardening, which may be seen as a high-entropy effect.
- Different heat treatments increase the strength of the $Ni_{44}Fe_{20}Cr_{20}Al_{16}$ and $Ni_{34.4}Fe_{16.4}Co_{16.4}Cr_{16.4}Al_{16.4}$ alloys at the expense of ductility. Embrittlement was recorded for the $Ni_{44}Fe_{20}Cr_{20}Al_{16}$ alloy after heat treatment at 750°C for 24 h, which could be attributed to a covering layer of Cr-rich precipitates along the interfacial boundaries. The annealing treatment at 950°C for 15 h was identified as a feasible option to improve the overall mechanical strength of the two high-entropy alloys.

To summarize, we saw a demonstrable improvement of mechanical properties and, most importantly, the work-hardening behavior when moving from the $Ni_{48}Fe_{34}Al_{18}$ to the $Ni_{44}Fe_{20}Cr_{20}Al_{16}$ and $Ni_{34.4}Fe_{16.4}Co_{16.4}Cr_{16.4}Al_{16.4}$ alloys, that is, upon the introduction of Cr and Co. From todays perspective, the $Ni_{44}Fe_{20}Cr_{20}Al_{16}$ Co-free alloy may constitute further advantages, such as corrosion resistance due to it's high Cr content, or societal and economic considerations that favor Co-free materials (Tkaczyk et al., 2018). When comparing the $Ni_{44}Fe_{20}Cr_{20}Al_{16}$ and $Ni_{34.4}Fe_{16.4}Co_{16.4}Cr_{16.4}Al_{16.4}$ alloys, attention has to be given to the covering layer of Cr-rich precipitates along the interfacial boundaries, which appears in quaternary samples after annealing at 750°C. This effect could be mitigated by applying heat treatment at 950°C. Under these conditions, the flexural yield strength reached 1,094 MPa and 12.5% flexural strain at fracture for the quaternary and 1,021 MPa and 15.6% flexural strain at fracture for the $Ni_{34.4}Fe_{16.4}Co_{16.4}Cr_{16.4}Al_{16.4}$ samples.

This study concludes that both the $Ni_{44}Fe_{20}Cr_{20}Al_{16}$ and $Ni_{34.4}Fe_{16.4}Co_{16.4}Cr_{16.4}Al_{16.4}$ eutectic alloys proposed by Jin and Gao (Gao et al., 2017; Jin et al., 2019) can be understood as a continuation of the earlier work by Misra and Gibala (Misra and Gibala, 1997; Misra and Gibala, 1999; Misra et al., 1998). The eutectic alloys provide good strength, work hardening ability, and the potential to further improve upon those properties by heat treatment. Depending on the targeted use, the room-temperature ductility of the $Ni_{44}Fe_{20}Cr_{20}Al_{16}$ eutectic may be sufficient such that the benefits related to the Co-free composition can be garnered. Further research on the processability of the two alloys are expected to lead to technical applications.

DATA AVAILABILITY STATEMENT

The raw data supporting the conclusions of this article will be made available by the authors, without undue reservation.

AUTHOR CONTRIBUTIONS

DR: writing of the manuscript, analysis of all experimental results, and scientific coordination; NN: arc melting and suction casting of samples; OS: SEM analysis and three-point bending experiments of selected samples; FS, PP, and DM: nano-indentation measurements and analysis; AG: Bridgman solidification and microstructure analysis of samples from the $Ni_{34.4}Fe_{16.4}Co_{16.4}Cr_{16.4}Al_{16.4}$ alloy, work performed as visiting scientist at Access e.V.; UH: design of the study, EBSD analysis of selected samples, scientific supervision, and revision of the manuscript.

FUNDING

This study was conducted within the publicly funded research framework INNO-KOM (Project EVERAM: 49VF180027). Funding by the German Ministry of Economics and Energy (BMWi) is gratefully acknowledged.

ACKNOWLEDGMENTS

The authors would like to thank Klemens Kelm and Frederic Kreps (Institut für Werkstoff-Forschung, DLR, Köln, Germany) for the TEM analysis and interpretation, and Christoph Pickmann for the conduction and technical supervision of directional solidification experiments in the Bridgman furnace.

REFERENCES

Bei, H., and George, E. P. (2005). Microstructures and mechanical properties of a directionally solidified NiAl-Mo eutectic alloy. *Acta Mater.* 53, 69. doi:10.1016/j.actamat.2004.09.003

Bhattacharjee, T., Wani, I. S., Sheikh, S., Clark, I. T., Okawa, T., Guo, S., et al. (2018). Simultaneous strength-ductility enhancement of a nano-lamellar $AlCoCrFeNi_{2.1}$ eutectic high entropy alloy by cryo-rolling and annealing. *Sci. Rep.* 8, 3276. doi:10.1038/s41598-018-21385-y

Cantor, B., Chang, I. T. H., Knight, P., and Vincent, A. J. B. (2004). Microstructural development in equiatomic multicomponent alloys. *Mater. Sci. Eng. A* 375–377, 213–218. doi:10.1016/j.msea.2003.10.257

Chen, T. K., Shun, T. T., Yeh, J. W., and Wong, M. S. (2004). Nanostructured nitride films of multi-element high-entropy alloys by reactive DC sputtering. *Surf. Coating. Technol.* 188–189, 193–200. doi:10.1016/j.surfcoat.2004.08.023

Drevermann, A., Pickmann, C., Sturz, L., and Zimmermann, G. (2004). "Observation and control of solidification processes by ultrasonic pulse-echo technique," in Proceedings of the IEEE ultrasonics symposium, Montreal, Quebec, Canada, September, 2004, Vol. 1, 537–540. (IEEE: New York, NY, USA). Available at: https://www.researchgate.net/publication/4134555 (Accessed September, 2004) [abstract].

Duncan, A. J., Kaufman, M. J., Liu, C. T., and Miller, M. K. (1994). Site occupation of iron in intermetallic NiAl. *Appl. Surf. Sci.* 76–77, 155–159. doi:10.1016/0169-4332(94)90336-0

Gao, X., Lu, Y., Zhang, B., Liang, N., Wu, G., Sha, G., et al. (2017). Microstructural origins of high strength and high ductility in an $AlCoCrFeNi_{2.1}$ eutectic high-entropy alloy. *Acta Mater.* 141, 59–66. doi:10.1016/J.ACTAMAT.2017.07.041

Hu, L., Zhang, G., Hu, W., Gottstein, G., Bogner, S., and Bührig-Polaczek, A. (2013). Tensile creep of directionally solidified NiAl-9Mo in situ composites. *Acta Mater.* 61, 7155–7165. doi:10.1016/j.actamat.2013.08.017

Jin, X., Bi, J., Zhang, L., Zhou, Y., Du, X., Liang, Y., et al. (2019). A new $CrFeNi_2Al$ eutectic high entropy alloy system with excellent mechanical properties. *J. Alloys Compd.* 770, 655. doi:10.1016/j.jallcom.2018.08.176

Jones, I. P. (2003). Determining the locations of chemical species in ordered compounds: ALCHEMI. *Adv. Imag. Electron. Phys.* 125, 63. doi:10.1016/S1076-5670(02)80015-5

Kurdjumow, G., and Sachs, G. (1930). Über den Mechanismus der Stahlhärtung. *Z. Phys.* 64, 325–343. doi:10.1007/BF01397346

Li, H., Cao, Y., Zhou, S., Zhu, P., and Zhu, J. (2016). Site preferences and effects of X (X = Mn, Fe, Co, Cu) on the properties of NiAl: a first-principles study. *Mod. Phys. Lett. B* 30, 1650129–1650133. doi:10.1142/S0217984916501335

Liu, C. T. (1995). Recent advances in ordered intermetallics. *Mater. Chem. Phys.* 42, 77–86. doi:10.1016/0254-0584(95)01546-9

Lu, Y., Dong, Y., Guo, S., Jiang, L., Kang, H., Wang, T., et al. (2014). A promising new class of high-temperature alloys: eutectic high-entropy alloys. *Sci. Rep.* 4, 6200. doi:10.1038/srep06200

Medvedeva, N. I., Gornostyrev, Y. N., Novikov, D. L., Mryasov, O. N., and Freeman, A. J. (1998). Ternary site preference energies, size misfits and solid solution hardening in NiAl and FeAl. *Acta Mater.* 46, 3433–3442. doi:10.1016/S1359-6454(98)00042-1

Miracle, D. B. (1993). Overview No. 104 the physical and mechanical properties of NiAl. *Acta Metall. Mater.* 41, 649–684. doi:10.1016/0956-7151(93)90001-9

Miracle, D. B., and Senkov, O. N. (2017). A critical review of high entropy alloys and related concepts. *Acta Mater.* 122, 448–511. doi:10.1016/J.ACTAMAT.2016.08.081

Misra, A., and Gibala, R. (1997). Room-temperature deformation behavior of directionally solidified multiphase Ni-Fe-Al alloys. *Metall. Mater. Trans.* 28, 795–807. doi:10.1007/s11661-997-0066-x

Misra, A., and Gibala, R. (1999). Slip transfer and dislocation nucleation processes in multiphase ordered Ni-Fe-Al alloys. *Metall. Mater. Trans.A* 30, 991–1001. doi:10.1007/s11661-999-0152-3

Misra, A., Hirth, J. P., and Hoagland, R. G. (2005). Length-scale-dependent deformation mechanisms in incoherent metallic multilayered composites. *Acta Mater.* 53, 4817–4824. doi:10.1016/J.ACTAMAT.2005.06.025

Misra, A., Wu, Z. L., Kush, M. T., and Gibala, R. (1998). Deformation and fracture behaviour of directionally solidified NiAl-Mo and NiAl-Mo(Re) eutectic composites. *Philos. Mag. A* 78, 533–550. doi:10.1080/01418619808241921

Nagase, T., Takemura, M., Matsumuro, M., and Maruyama, T. (2017). Solidification microstructure of $AlCoCrFeNi_{2.1}$ eutectic high entropy alloy ingots. *J. Japan Foundry Eng. Soc.* 89, 119–129. doi:10.11279/jfes.89.119

Newbury, D. E., and Ritchie, N. W. M. (2013). Is scanning electron microscopy/energy dispersive X-ray Spectrometry (SEM/EDS) quantitative? *Scanning* 35, 141–168. doi:10.1002/sca.21041

Noebe, R. D., Bowman, R. R., and Nathal, M. V. (1993). Physical and mechanical properties of the B2 compound NiAl. *Int. Mater. Rev.* 38, 193–232. doi:10.1179/imr.1993.38.4.193

Oliver, W. C., and Pharr, G. M. (1992). An improved technique for determining hardness and elastic modulus using load and displacement sensing indentation experiments. *J. Mater. Res.* 7, 1564–1583. doi:10.1557/JMR.1992.1564

Plapp, M., and Karma, A. (2002). Eutectic colony formation: a phase-field study. *Phys. Rev. E* 66, 61608. doi:10.1103/PhysRevE.66.061608

Qian, L., Li, M., Zhou, Z., Yang, H., and Shi, X. (2005). Comparison of nano-indentation hardness to microhardness. *Surf. Coating. Technol.* 195, 264–271. doi:10.1016/j.surfcoat.2004.07.108

Raheem, Z. (2019). Standard test methods for flexural properties of unreinforced and reinforced plastics and electrical insulating materials. *J. Test. Eval.* 1. doi:10.1520/D0790-02

Schneider, C. A., Rasband, W. S., and Eliceiri, K. W. (2012). NIH Image to ImageJ: 25 years of image analysis. *Nat. Methods* 9, 671–675. doi:10.1038/nmeth.2089

Shang, Z., Shen, J., Zhang, J., Wang, L., and Fu, H. (2012). Effect of withdrawal rate on the microstructure of directionally solidified NiAl-Cr(Mo) hypereutectic alloy. *Intermetallics* 22, 99–105. doi:10.1016/j.intermet.2011.10.018

Shen, Z., Wagoner, R. H., and Clark, W. A. T. (1988). Dislocation and grain boundary interactions in metals. *Acta Metall.* 36, 3231–3242. doi:10.1016/0001-6160(88)90058-2

Tkaczyk, A. H., Bartl, A., Amato, A., Lapkovskis, V., and Petranikova, M. (2018). Sustainability evaluation of essential critical raw materials: Cobalt, Niobium, Tungsten and rare earth elements. *J. Phys. D. Appl. Phys.* 51, 203001. doi:10.1088/1361-6463/aaba99

Wang, L., Shen, J., Shang, Z., and Fu, H. (2014). Microstructure evolution and enhancement of fracture toughness of NiAl-Cr(Mo)-(Hf,Dy) alloy with a small addition of Fe during heat treatment. *Scr. Mater.* 89, 1–4. doi:10.1016/j.scriptamat.2014.07.002

Wang, L., Shen, J., Zhang, Y., Guo, L., Xu, H., and Fu, H. (2017). Microstructure evolution and room temperature fracture toughness of as-cast and directionally solidified novel NiAl-Cr(Fe) alloy. *Intermetallics* 84, 11–19. doi:10.1016/j.intermet.2016.12.021

Wang, L., Yao, C., Shen, J., Zhang, Y., Wang, T., Ge, Y., et al. (2020). Microstructures and room temperature tensile properties of as-cast and directionally solidified $AlCoCrFeNi_{2.1}$ eutectic high-entropy alloy. *Intermetallics* 118, 106681. doi:10.1016/j.intermet.2019.106681

Wang, L., Yao, C., Shen, J., Zhang, Y., Wang, T., Xu, H., et al. (2019). Microstructures and compressive properties of NiAl-Cr(Mo) and NiAl-Cr eutectic alloys with different Fe contents. *Mater. Sci. Eng. A* 744, 593–603. doi:10.1016/j.msea.2018.12.085

Wang, W.-R., Wang, W.-L., Wang, S.-C., Tsai, Y.-C., Lai, C.-H., and Yeh, J.-W. (2012). Effects of Al addition on the microstructure and mechanical property of AlxCoCrFeNi high-entropy alloys. *Intermetallics* 26, 44–51. doi:10.1016/j.intermet.2012.03.005

Wani, I. S., Bhattacharjee, T., Sheikh, S., Bhattacharjee, P. P., Guo, S., and Tsuji, N. (2016). Tailoring nanostructures and mechanical properties of $AlCoCrFeNi_{2.1}$ eutectic high entropy alloy using thermo-mechanical processing. *Mater. Sci. Eng. A* 675, 99–109. doi:10.1016/j.msea.2016.08.048

Conflict of Interest: FS, PP, and DM were employed by the company Anton Paar Germany GmbH.

The remaining authors declare that the research was conducted in the absence of any commercial or financial relationships that could be construed as a potential conflict of interest.